Ionics (2019) 25:4341–4350
https://doi.org/10.1007/s11581-019-02980-z

ORIGINAL PAPER

Low-cost high-performance asymmetric supercapacitors based on ribbon-like $Ni(OH)_2$ and biomass carbon nanofibers enriched with nitrogen and phosphorus

Debin Kong[1] · Lin Cao[1] · Zeming Fang[1] · Fenglin Lai[1] · Zhidan Lin[1] · Peng Zhang[1] · Wei Li[1]

Received: 3 January 2019 / Revised: 3 March 2019 / Accepted: 21 March 2019 / Published online: 3 May 2019

Abstract

Herein, we report a facile and low-cost synthesis of nitrogen and phosphorus co-doped carbonized bacterial cellulose (N, P-CBC) via in-situ soaking bacteria cellulose and carbonization method. The N, P-CBC yielded a high specific capacitance of 232 F g^{-1} at 1 A g^{-1} and 92.7% rate capability retention at 5 A g^{-1}. Moreover, the asymmetric supercapacitor (ASC) device was further fabricated with N, P-CBC as the negative electrode and $Ni(OH)_2$, prepared using a simple chemical precipitate method as the positive electrode. The fabricated ASC device provided a maximum working voltage of 1.6 V and high energy density (41.9 Wh kg^{-1} at a power density of 799.2 W kg^{-1}). The device exhibits remarkable specific capacitance (118 F g^{-1} at 1 A g^{-1}) and excellent cycle lifetime (76.3% specific capacitance after 5000 cycles). Such an excellent electrochemical performance demonstrated that the as-prepared N, P-CBC and $Ni(OH)_2$ electrodes will be both great potential candidates for supercapacitors.

Keywords Nitrogen and phosphorus co-doped · Carbonized bacterial cellulose · $Ni(OH)_2$ · Asymmetric supercapacitors

Introduction

Serious increase in environmental pollution and energy crisis all over the world makes it urgently necessary for the development of eco-friendly and renewable energy storage devices. Compared with batteries, supercapacitors, as another promising energy storage device, are capturing tremendous attention due to their excellent electrochemical stability, rapid charge–discharge cycle capability, ultrahigh power characteristics, and fine cycling performance [1–4]. However, relatively low energy density (E) of supercapacitors [5, 6], which is limited to the capacitance (C) of the electrodes and their operating voltage (V) according to the formula of $E = 1/2CV^2$, is still regarded as a very important drawback. For instance, the working voltage of symmetric supercapacitors (ASC) using aqueous electrolytes is limited to below 1.23 V owing to the decomposition potential window of water [7]. Therefore, a number of researches [8–14] have recently been carried out on asymmetric or hybrid supercapacitors with high operating potential window and energy density while sustaining remarkable power density and cycle lifetime. In brief, this ASC can be made up of carbon-based materials, the negative electrode materials (exhibiting a double-layer capacitive), and the pseudocapacitance or battery-type materials using fast and reversible faradic surface redox reaction to store energy as positive electrode [15]. Thus, it is a feasible approach to obtain a supercapacitor with high energy density via a selection of appropriate electrode materials [16].

As for the positive electrode in a capacitor, nickel hydroxide [$Ni(OH)_2$] is a very promising electrode material with many attractive features, including excellent redox behavior and high theoretical capacitance value [17]. It can be easily synthesized at low production cost, is non-toxic, and environmentally friendly, while has been intensively studied for a long time. The synthesis methods of $Ni(OH)_2$, such as

✉ Zhidan Lin
linzd@jnu.edu.cn

✉ Peng Zhang
tzhangpeng@jnu.edu.cn

[1] Institute of Advanced Wear & Corrosion Resistant and Functional Materials, Jinan University, Guangzhou 510632, People's Republic of China

electroplating [18, 19], chemical bath precipitation [20, 21], hydrothermal [22, 23], and microwave-assisted [24] methods have been reported, and the products were successfully prepared with unique morphology and favorable capacitive performance.

On the other hand, biomass carbon materials possess several advantages, such as low cost, environmentally friendly, ultra-high specific surface area, and excellent cycle performance [25, 26]. Because of these attractive characteristics, they can be considered as suitable materials for the negative electrode in an asymmetric supercapacitor. However, the amount of biomass carbon materials has unfavorable properties of hydrophilicity, poor conductivity, and low specific capacity. Thus, there were great efforts to improve the specific capacity of carbon materials by two major ways of activated processing [27, 28] and doping modification [29–31]. Many studies manifest that heteroatoms (N, S, O, P) doped into carbon materials not only can improve the electrical conductivity but enhance the wettability character, which facilitates the contact between electrode and electrolyte. Moreover, by introducing functional groups on the surface, the heteroatoms-doped carbon materials could contribute further on pseudocapacitance property owing to the redox reactions in addition to the electric double-layer capacitance of carbon material itself.

In the present work, we fabricated a low-cost and high-performance ASC device based on nitrogen and phosphorus co-doped carbonized bacterial cellulose(N, P-CBC) using $(NH_4)_2HPO_4$ as dopant source via in situ immersion and pyrolysis method as negative electrode, and $Ni(OH)_2$, synthesized through chemical precipitation, as positive electrode. The fabricated $Ni(OH)_2$ //N, P-CBC ASC device exhibited outstanding electrochemical characters in 6 M KOH electrolyte, containing the working voltage window (1.6 V), the maximum energy density (41.9 Wh kg^{-1} at power density of 799.2 W kg^{-1}), and 76.3% capacitance retention after 5000 cycles.

Experimental

Materials

The bacterial cellulose (BC, $320 \times 240 \times 3$ mm^3) were purchased from Hainan Yide Food Co. Ltd., China. Diammonium hydrogen phosphate [$(NH_4)_2HPO_4$] and sodium hydroxide (NaOH) were purchased from Tianjin Damao Chemical Reagent Company. Nickel nitrate hexahydrate [$Ni(NO_3)_2{\cdot}6H_2O$] was purchased from Guangzhou Chemical Reagent Company. All chemicals used in this present work were of analytic reagent grade and used without any further purification.

Preparation of N, P-CBC negative materials

The pre-treated bacterial cellulose (BC) slices were immersed in 100 mL $(NH_4)_2HPO_4$ solution (0.025 M), agitated at room temperature for 12 h. Afterward, these pellicles were treated pre-frozen with liquid nitrogen and lyophilized. Finally, the BC/$(NH_4)_2HPO_4$ freeze-dried samples were carbonized under N_2 atmosphere at 800 °C, and named as N, P-CBC. Moreover, the pure carbonized bacterial cellulose (CBC) was prepared following the same method without adding dopant agents.

Preparation of $Ni(OH)_2$ positive materials

Nickel hydroxide was synthesized through chemical precipitation method. In a typical experiment, 50 mL $Ni(NO_3)_2$ $6H_2O$ solution (0.5 M) was quickly added into 100 mL NaOH solution (3 M). The reaction was carried out for 10 min in a microwave apparatus (M1-L213B, Midea, 700 W). After that, the obtained green precipitate was washed several times with distilled water, collected through filtration, and dried at 60 °C for 12 h.

Assembly of an asymmetric supercapacitor device

The $Ni(OH)_2$//N, P-CBC asymmetric supercapacitor device was prepared with $Ni(OH)_2$ and N, P-CBC as positive and negative electrodes, respectively. An MPF 30 AC-100 (NKK) membrane and 6 M KOH solution were used as separator and electrolyte, respectively. The mass ratio of the positive and negative electrode was adjusted at 0.99.

Materials characterization

The microstructures of the materials were characterized using field emission scanning electron microscope (FESEM, ZEISS Ultra55) and transmission electron microscope (TEM, JEOL JEM-2100F). The phase structures were determined with an X-ray diffractometer (XRD, Rigaku Ultima IV, Cu Kα, λ = 0.1542 nm, 40 kV, 40 mA). X-ray photoelectron spectroscopy (XPS) examination was performed using ESCALab250 spectrometer with Al Kα radiation (hν = 1486.6 eV). Specific surface area and pore size characteristics were examined using the nitrogen adsorption technique with 3H-2000PS1/2 (BeiShiDe Instrument, China) analytical instrument.

Preparation of electrode and electrochemical measurement

The electrochemical performances were examined using a three-electrode system in 6 mol L^{-1} KOH solution electrolyte using an electrochemical working station (Princeton P4000, USA). Hg/HgO or saturated calomel electrode was used as the reference electrode and Pt electrode was used counter

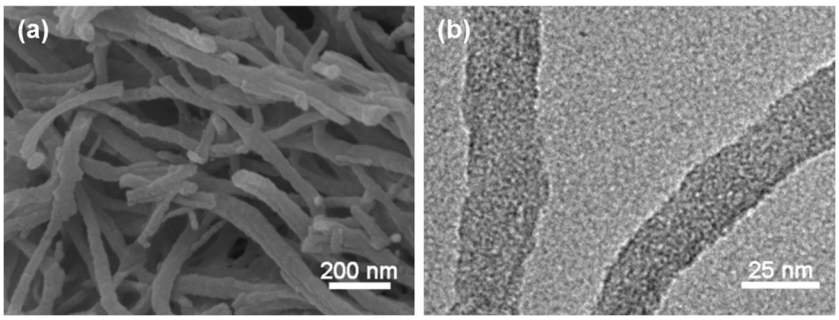

Fig. 1 **a** SEM image of N, P-CBC. **b** TEM image of N, P-CBC

electrode, respectively. The working electrode was fabricated via mixing as-synthesized product, carbon black, and 5% PTFE (polytetrafluoroethylene) with a mass ratio of 8:1:1 in anhydrous ethanol. The mixture was dip-coated on a 1 cm × 1 cm nickel foam and dried for 12 h at 100 °C. The loading mass of the electrode was about 1~2 mg. Cyclic voltammogram (CV) characteristics were determined at different scan rates within the potential range of − 1.0~0 V for N, P-CBC electrode and − 0.1~0.6 V for $Ni(OH)_2$ electrode, respectively. Galvanostatic charge–discharge (GCD) was obtained at a variety of current densities from − 1.0 to 0 V for N, P-CBC electrode and from 0 to 0.4 V for $Ni(OH)_2$ electrode, respectively. The electrochemical impedance spectroscopy (EIS) examination was performed in a frequency range of 10 mHz to 100 kHz under an AC voltage of 5 mV.

Results and discussion

After adequate immersion in $(NH_4)_2HPO_4$ solution, the bacteria cellulose slices adsorbed enough $(NH_4)_2HPO_4$ due to their porous structure. N, P-CBC sample was prepared

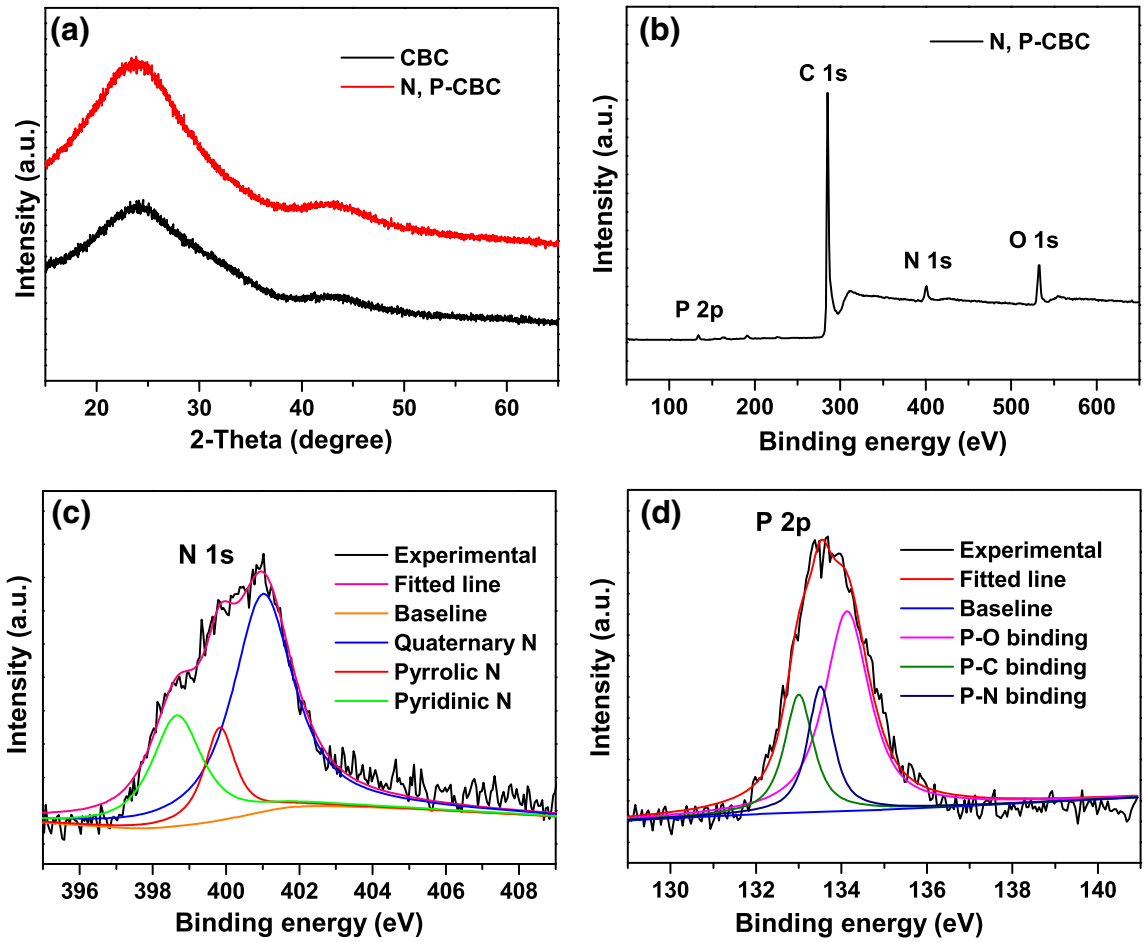

Fig. 2 **a** XRD patterns of CBC and N, P-CBC. **b** XPS survey spectrum of N, P-CBC. **c** High-resolution N 1 s spectra of N, P-CBC. **d** High-resolution P 2p spectra of N, P-CBC

through the carbonization of BC/$(NH_4)_2HPO_4$. The SEM micrograph (Fig. 1a) shows the morphology of N, P-CBC composing several nanometer-sized fibers with a three-dimensional (3D) network structure including abundant interconnected pores. It can provide a high specific surface area that enhances electron and ion transportation. Moreover, the diameter of these nanofibers was observed at about 20–50 nm, as verified by the TEM micrograph shown in Fig. 1b.

The phase structures of carbonization products were analyzed with the XRD technique in a wide-angle region. As shown in Fig. 2a, two diffraction peaks located at 2θ of 25° and 43.54°, ascribed to (002) and (101) planes, verified the pyrolysis product as an amorphous carbon with low graphitization degree. XPS examination result revealed C, N, P, and O elements existing in the N, P-CBC sample, proving that nitrogen and phosphor are successfully introduced in the as-prepared sample (Fig. 2b). For the N 1 s emission spectrum (Fig. 2c), it yielded three peaks at 398.7, 399.7, and 401.2 eV, defined as pyridinic (N-6), pyrrolic (N-5), and quaternary nitrogen (N-Q) [32, 33]. In addition, the P 2p emission spectrum can be divided into three peaks as depicted in Fig. 2d. The peaks located at 133.0, 133.6, and 134.1 eV correspond to P–C, P–N, and P–O bindings [34].

To determine the porous structure of the sample, N_2 adsorption-desorption isotherm and pore size distributions curves were obtained at 77 K, as illustrated in Fig. 3 a and b. As N_2 adsorption-desorption isotherm curves of CBC and N, P-CBC (Fig. 3a) show, huge adsorption takes place at low relative pressures. At high relative pressures, the region appeared as a hysteresis loop, which implies the co-existence of micropores (< 2 nm) and mesopores (2–50 nm) in the two kinds of samples. Further detailed parameters of these specimens are listed in Table 1. The porous feature of N, P-CBC sample provides micropores and mesopores with an average pore size of 3.81 nm, revealed in Fig. 3b and Table 1. The samples of CBC and N, P-CBC provided specific surface areas of 516.26 and 731.90 $m^2\ g^{-1}$ (Fig. 3a and Table 1), respectively. The formation of these pores can be attributed to the release of volatile components, including H_2O, CO, CO_2, and others during the pyrolysis process of BC/$(NH_4)_2HPO_4$ precursor [35, 36]. The high specific surface area and porous structure offer more active sites that enhance electrochemical properties.

Table 1 Pore parameters of sample CBC and N, P-CBC

Sample	S_{BET} ($m^2\ g^{-1}$)	V_{total} ($cm^3\ g^{-1}$)	d_M (nm)
CBC	516.26	0.76	5.94
N, P-CBC	731.90	0.70	3.81

The electrochemical properties of N, P-CBC electrode materials were characterized using cyclic voltammetry (CV) and galvanostatic charge/discharge (GCD) examinations in a three-electrode system. The CV curves for CBC and N, P-CBC at a scan rate of 50 mV s^{-1} and a potential window from − 1.0 to 0 V are presented in Fig. 4a. Compared with the two CV plots, it can be obviously found that the plot area for N, P-CBC electrode is larger than that of pure CBC, indicating better electrochemical properties of N, P-CBC. This observation should be ascribed to the introduction of nitrogen and phosphorus elements into the carbon frameworks, which provides more pseudocapacitance. Furthermore, the effect of sweep speed on the electrochemical behavior of N, P-CBC electrode was also surveyed. Figure 4b displays the CV plots of N, P-CBC electrode at various scan rates from 10 to 200 mV s^{-1}. The CV curves exhibited quasi-rectangle shapes, indicating that this electrode material possesses excellent double-layer capacitance behavior. As the scan rate increases, the enclosed area of the curve increases; however, its shape still remains rectangular, reflecting its excellent rate performance.

Figure 4c shows GCD curves of N, P-CBC under various current densities of 1, 2, 3, 4, and 5 A g^{-1}. The GCD curves exhibit symmetrical triangular shapes, demonstrating that this carbon material possesses the characters of quick charge–discharge and low inner resistance. Various capacitive values gained from the GCD profiles based on CBC and N, P-CBC

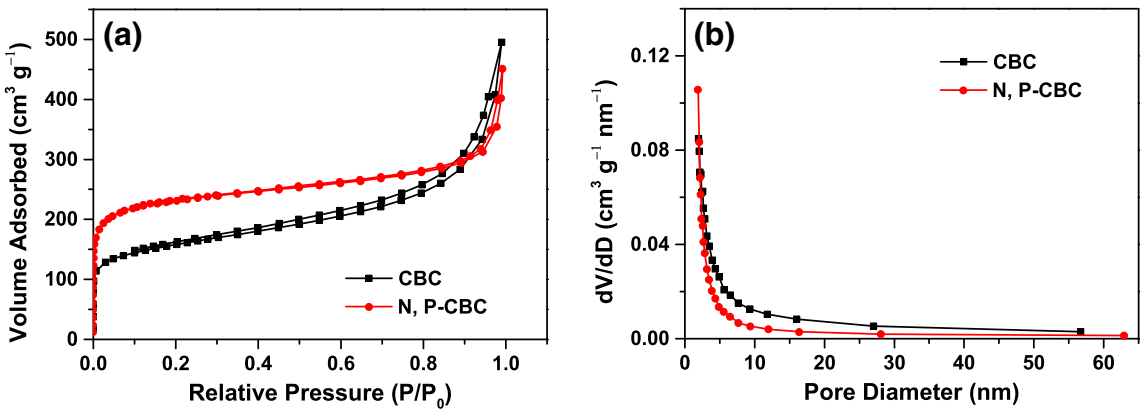

Fig. 3 **a** Nitrogen adsorption-desorption isotherms and **b** pore size distributions of CBC and N, P-CBC

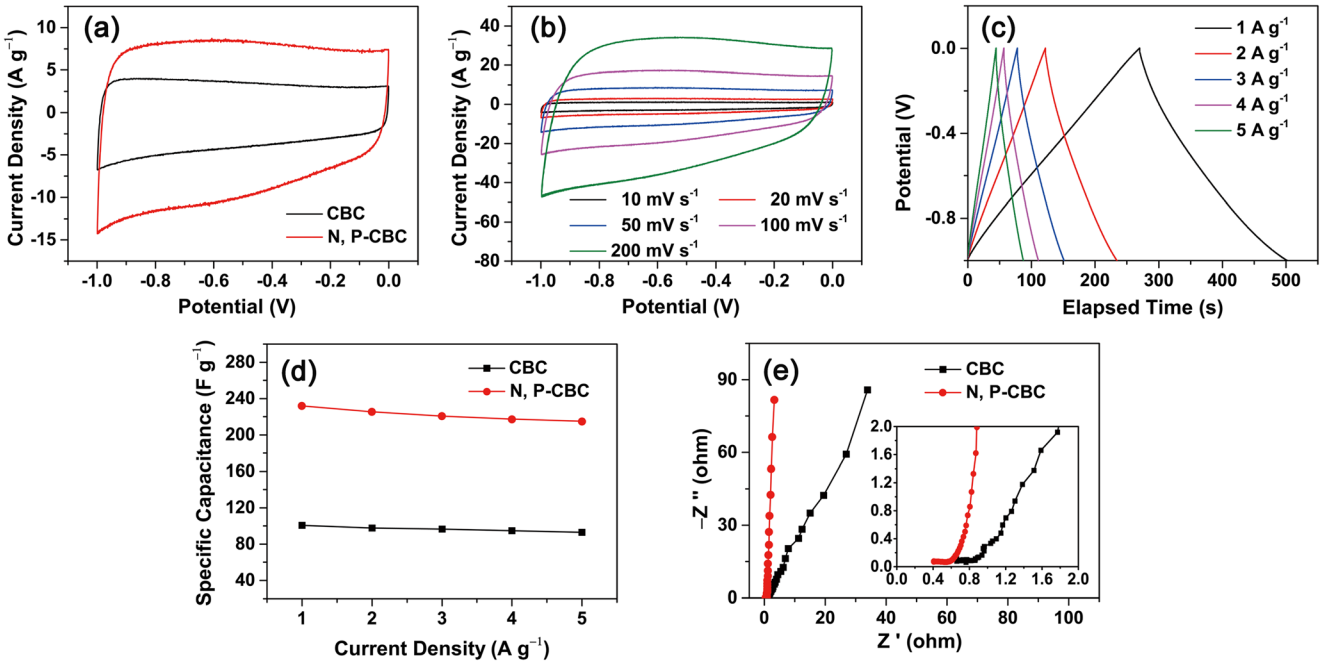

Fig. 4 **a** CV curves of CBC and N, P-CBC at the scan rate of 50 mV s^{-1}. **b** CV curves of N, P-CBC at different scan rates. **c** Charge-discharge curves of N, P-CBC. **d** Specific capacitance of N, P- CBC at varied current densities. **e** Nyquist plots of CBC and N, P-CBC electrodes

electrodes in 6 mol L^{-1} KOH aqueous solution are displayed in Fig. 4d. As the electric current density increased from 1 to 5 A g^{-1}, the CBC sample exhibited smaller specific capacitance values from 100 to 93 F g^{-1}; whereas, the N, P-CBC sample performed larger specific capacitance values from 232 to 215 F g^{-1}. Moreover, as depicted in Fig. 4d, N, P-CBC electrode achieved higher capacitance retention (92.7%) compared with CBC (92.3%) when the current density reached 5 A g^{-1}. The enhanced capacitive performance observed for the N, P-CBC electrode is due to nitrogen and phosphorus co-doping, which provides a larger specific surface area and further pseudo-capacitance.

To obtain a profound knowledge about the capacitance property of the re-prepared electrodes, electrochemical impedance spectroscopy (EIS) examinations were conducted. Figure 4e depicts the Nyquist plots of the electrodes based on pure CBC and N, P-CBC. The curves show quasi-semicircles in the high-frequency region, which is related to charge-transfer resistance (R_{ct}) and the axial intercept stands for the bulk resistance (R_s) [37]. The values of R_s for N, P-CBC was measured as approximately 0.4 Ω, which is smaller than that of CBC (0.6 Ω). This result also demonstrates that N, P co-doped can enhance the electrical conductivity, to some extent, improving the specific capacitance. At low frequencies, it can be noted that the straight line of the sample N, P-CBC is more vertical, which is closer to an ideal capacitor. In other words, the negative material of N, P-CBC exhibits much better supercapacitive performance.

For the fabrication of the positive electrode material, a simple chemical precipitation method was implemented to synthesis $Ni(OH)_2$ using NaOH as the precipitator. When nickel nitrate aqueous solution is added to NaOH solutions, OH^- ions in solution react with Ni^{2+}, producing $Ni(OH)_2$ precipitate. Figure 5 reveals the morphology of produced $Ni(OH)_2$ at both low and high magnifications, indicating ribbon-like morphology. The ribbons sizes varied from 200 to 500 nm in width.

Diagram resulted from XRD of $Ni(OH)_2$ powders (Fig. 6a) shows diffraction peaks at 2θ angle positions of 19.01°,

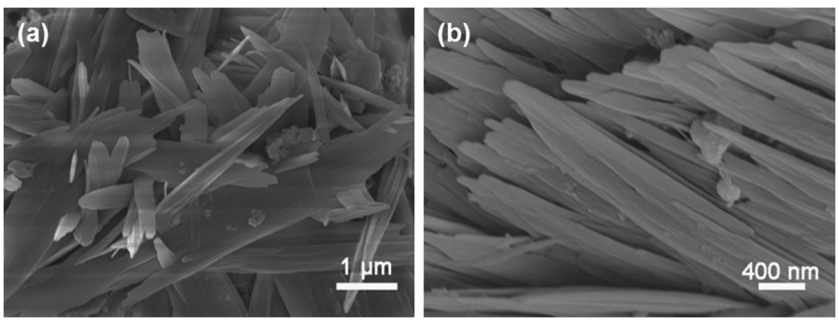

Fig. 5 **a**, **b** SEM images of $Ni(OH)_2$

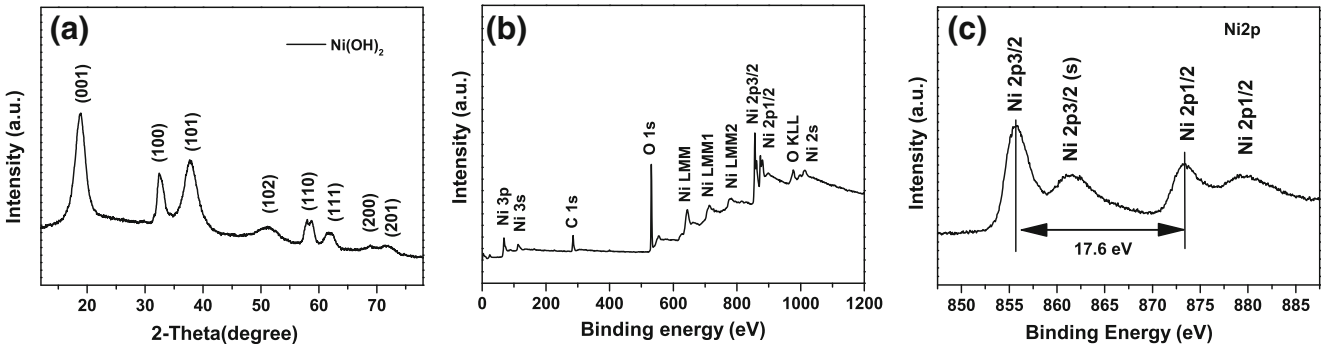

Fig. 6 **a** XRD spectrum of $Ni(OH)_2$. **b** XPS survey spectrum of $Ni(OH)_2$. **c** High-resolution Ni 2p spectra of $Ni(OH)_2$

32.98°, 38.10°, 51.56°, 58.84°, 62.18°, 68.66°, and 72.12°. These peaks can be assigned to (001), (100), (101), (102), (110), (111), (200), and (201) crystal planes, corresponding to the theophrastite phase of β-$Ni(OH)_2$ (JCPDS 14–0117). Moreover, Fig. 6b shows the XPS survey spectrum of $Ni(OH)_2$ in which it exhibits two major elements including O and Ni. For the high-resolution Ni 2p emission spectrum (Fig. 6c), two main peaks at 855.7 and 873.3 eV are identified as Ni 2p3/2 and Ni 2p1/2, respectively. The value of spinning energy separation was observed as about 17.6 eV, a typical characteristic of $Ni(OH)_2$ phase [38–40], which is consistent with the XRD results. Furthermore, the satellite peaks (879.8 and 861.6 eV) corresponding to Ni 2p1/2 and Ni 2p3/2 signals were also observed [39]. All of these pieces of evidence can confirm the successful synthesize of $Ni(OH)_2$.

The electrochemical studies of $Ni(OH)_2$ electrode were also performed using a three-electrode cell method. The CV profiles of $Ni(OH)_2$ electrode at various scanning rates from 5 to 50 mV s^{-1} are presented in Fig. 7a. The plots exhibit a pair of prominent oxidative and reductive peaks, implying that there is a faradic redox reaction related to Ni^{2+}/Ni^{3+} occurring in KOH aqueous solution, corresponding to faradic

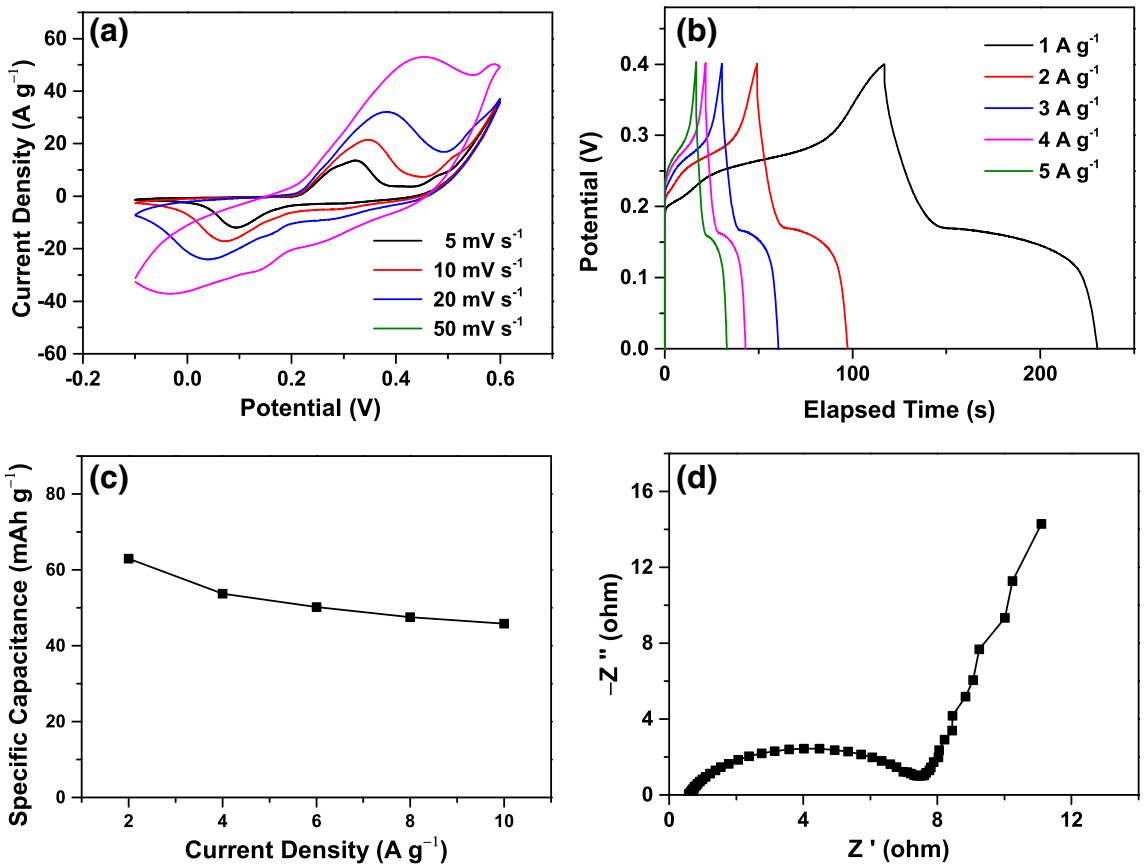

Fig. 7 **a** CV curves of $Ni(OH)_2$ at different scan rates. **b** Charge–discharge curves of $Ni(OH)_2$ at different current densities. **c** Specific capacitances of $Ni(OH)_2$ measured at various current densities. **d** Nyquist plot of $Ni(OH)_2$

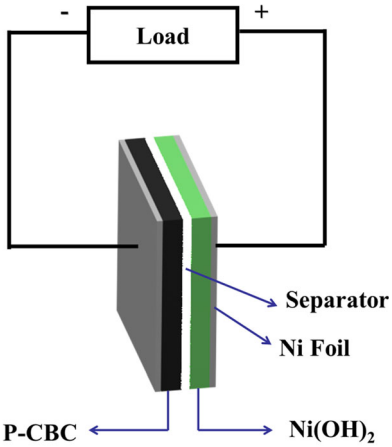

Fig. 8 Schematic of the assembled structure of an asymmetric supercapacitor based on $Ni(OH)_2$ positive electrode and N, P-CBC negative electrode

characteristics of battery-type electrode [40]. As the scanning rate was increased, the reduction peaks moved towards lower potential, and the oxidation peaks shifted to a higher potential, which may be due to the effect of polarization. The CV curves retain a similar shape, implying excellent capacitance and electrochemical reactivity of the material. The GCD curves for $Ni(OH)_2$ electrode at current densities from 2 to 10 A g^{-1} in the potential range of 0–0.4 V (Fig. 7b) present an obvious platform in the process of discharge. This observation also indicates a typical faradaic feature for the battery-type materials. The calculated specific capacitance was found as 63 mAh g^{-1} (ca. 567 F g^{-1}) at 2 A g^{-1}. Notably, the $Ni(OH)_2$ electrode performed well with a rate of 72.7% at 10 A g^{-1} of a high current density (Fig. 7c). The Nyquist plot of the $Ni(OH)_2$ electrode in Fig. 7d consists of a semicircular and linear region. The examination resulted in R_s value of 0.63 Ω. Such a positive electrode material with high-capacitance and well-capacitance rate is a promising candidate material for asymmetric supercapacitor devices.

To assess the practical application of the electrode materials, a hybrid asymmetric supercapacitor (ASC) was assembled with $Ni(OH)_2$ and N, P-CBC as the positive and negative electrode, depicted in Fig. 8, named as $Ni(OH)_2$//N, P-CBC. From the GCD curves of N, P-CBC (Fig. 4c) and $Ni(OH)_2$ (Fig. 7b), the capacitance value for N, P-CBC was measured as 225 F g^{-1} at 2 A g^{-1} in a voltage window from − 1.0 to 0 V, while that of $Ni(OH)_2$ is 63 mAh g^{-1} (567 F g^{-1}) at 2 A g^{-1} in a voltage range of 0–0.4 V. Consequently, the optimal mass ratio was calculated as m $[Ni(OH)_2]$/m [N, P-CBC] = 0.99 in the ASC device.

Figure 9a presents the CV plots of $Ni(OH)_2$ electrode (− 0.1 to 0.6 V) and N, P-CBC electrode (− 1.0 to 0 V) measured with a three-electrode system at a scanning rate of 20 mV s^{-1}. Therefore, the operating potential window for $Ni(OH)_2$//N, P-CBC ASC device can be broadened to 1.6 V. Figure 9b reveals the CV profiles at a scanning rate of 50 mV s^{-1} for $Ni(OH)_2$// N, P-CBC supercapacitor at various potential windows from

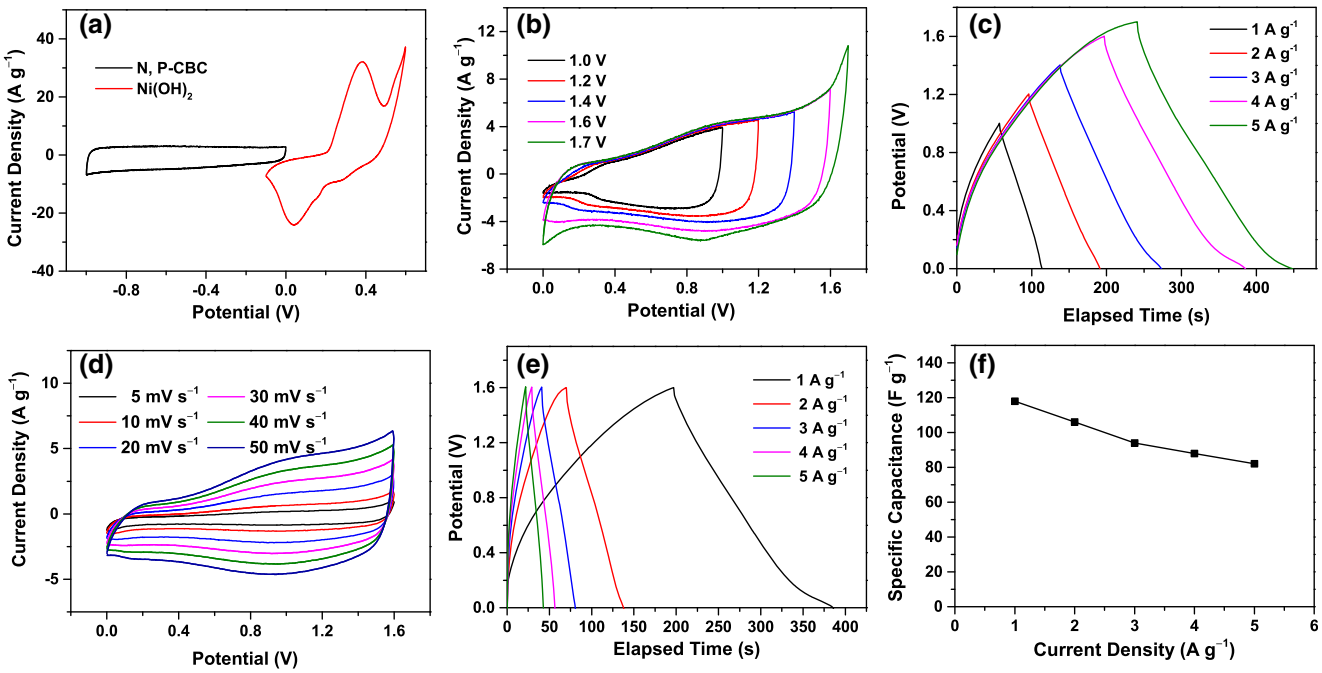

Fig. 9 **a** CV plots of N, P-CBC and $Ni(OH)_2$ electrodes performed in a three-electrode cell in 6 M KOH electrolyte at a scan rate of 20 mV s^{-1}. **b** CV curves of $Ni(OH)_2$//N, P-CBC ASC device tested at different potential windows at the same scan rate of 50 mV s^{-1}. **c** CP curves of $Ni(OH)_2$//N, P-CBC ASC device tested at different potential windows at the same current density of 1 A g^{-1}. **d** CV curves of $Ni(OH)_2$//N, P-CBC ASC device at different scan rates. **e** Charge–discharge curves of $Ni(OH)_2$//N, P-CBC ASC device at different current densities. **f** Specific capacitance value of $Ni(OH)_2$//N, P-CBC ASC device at different current densities

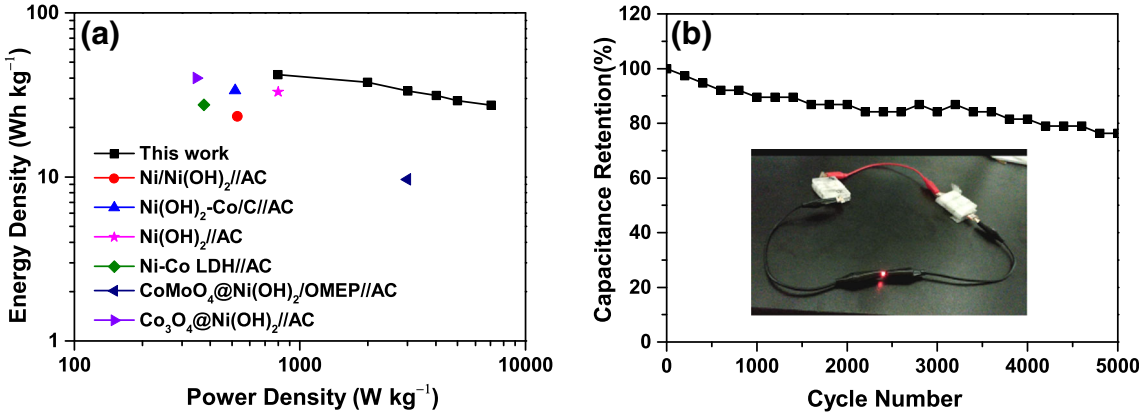

Fig. 10 **a** Ragone plots relating power density to energy density of $Ni(OH)_2$//N, P-CBC ASC device. **b** Long-term cycling performance at 5 A g^{-1} for $Ni(OH)_2$//N, P-CBC ASC device (inset: photographs of the device of $Ni(OH)_2$//N, P-CBC ASC devices powered a red LED)

1.0 to 1.7 V. When the potential window reached to 1.7 V, the shape of the CV curve changed, indicating obvious polarization due to the oxygen evolution reaction. To further explore the potential window, the CP curves at a current density of 1 A g^{-1} for $Ni(OH)_2$//N, P-CBC supercapacitor at various potential windows from 1.0 to 1.7 V were tested (Fig. 9c). The coulombic efficiency of the CP curve measured between 0 and 1.6 V is approximately 95.94%; however, the coulombic efficiency dropped to 86.31% when the potential window reaches 1.7 V. Based on these observations, the working potential window of this device was chosen as 1.6 V. The CV plots of $Ni(OH)_2$//N, P-CBC supercapacitor at various scanning rates under a potential window of 0–1.6 V are exhibited in Fig. 9d. These CV plots show irregular rectangles, demonstrating that the electrochemical performance is dominated by both electrical double-layer capacitive and faradaic characteristics. The CV shape did not change at different scanning rates, suggesting excellent capacitive behavior by the ASC device. The GCD curves measured at various current densities (Fig. 9e) are almost symmetric to each other, implying the reversible capacitive performance.

The specific capacitance for $Ni(OH)_2$//N, P-CBC ASC device was calculated as 118 F g^{-1} at a current density of 1 A g^{-1} in 6 mol L^{-1} KOH aqueous solution. A high capacitance retention of 69.5% was determined from Fig. 9f. The obtained Ragone plot compared with the previous report about asymmetric supercapacitor devices is exhibited in Fig. 10a and Table 2. The fabricated $Ni(OH)_2$//N, P-CBC supercapacitor provided a high energy density of 41.9 Wh kg^{-1} at a power density of 799.2 W kg^{-1} and a high power density of 4998.9 W kg^{-1} at an energy density of 29.2 Wh kg^{-1}, which are much greater values than the reported ones [41–46]. In addition, the $Ni(OH)_2$//N, P-CBC supercapacitor device still maintained 76.3% of capacitance retention at 5 A g^{-1} after 5000 cycles (Fig. 10b), offering good cycle performance. The inset in Fig. 10b displays the red light-emitting diode that was successfully powered using two ASCs in series, demonstrating its great potential application in energy storage. The LED could be lit for 5 min after charged for only 20 s. Therefore, the above superior electrochemical performance indicates that this asymmetric supercapacitor device assembled by $Ni(OH)_2$ and N, P-CBC electrodes is a good potential candidate for energy storage applications.

Conclusion

In summary, nitrogen and phosphorus co-doped carbonized bacterial cellulose (N, P-CBC) were synthesized through immersing and carbonizing method, exhibiting a remarkable

Table 2 Comparative energy density of $Ni(OH)_2$//N, P-CBC ASC and other materials from previous reports

Material	Energy density (Wh kg^{-1})	Power density (W kg^{-1})	Ref. (year)
Ni/Ni(OH)$_2$//AC	23.5	530	[41] (2017)
Ni(OH)$_2$-Co/C//AC	33.6	516.3	[42] (2019)
Ni(OH)$_2$//AC	32.9	800	[43] (2018)
Ni-Co LDH//AC	27.5	375	[44] (2017)
CoMoO$_4$@Ni(OH)$_2$/OMEP//AC	9.7	3000	[45] (2018)
Co$_3$O$_4$@Ni(OH)$_2$//AC	40.0	346.9	[46] (2017)
Ni(OH)$_2$//N, P-CBC	41.9	799.2	This work

specific capacitance (232 F g^{-1} at 1 A g^{-1}). Meanwhile, $Ni(OH)_2$ was also easily prepared via chemical precipitation method under microwave with a capacitance of 63 mAh g^{-1} at a current density 2 A g^{-1}. A high-performance hybrid asymmetric supercapacitor (ASC) device at relatively low cost was fabricated with $Ni(OH)_2$ as a positive electrode and N, P-CBC as the negative electrode. The fabricated device provided high specific energy density (41.9 Wh kg^{-1} at a power density of 799.2 W kg^{-1}) and good cycling performance (76.3% of capacitance retention at 5 A g^{-1} after 5000 cycles). By this approach, inexpensive electrode materials with outstanding electrochemical performance can be fabricated and applied for energy storage.

Funding information This research was supported by the Guangdong Science and Technology Project Fund (no. 2015A030310488) and the Scientific Cultivation and Innovation Fund Project of Jinan University (Nos. 21617427 and 21617422).

References

1. Wang YG, Song YF, Xia YY (2016) Electrochemical capacitors: mechanism, materials, systems, characterization and applications. Chem Soc Rev 45:5925–5950
2. Winter M, Ralph J, Brodd (2004) What are batteries, fuel cells, and supercapacitors? Chem Rev 104:4245–4270
3. Simon P, Gogotsi Y (2008) Materials for electrochemical capacitors. Nat Mater 7:845–854
4. Chen HC, Jiang JJ, Zhang L, Zhao YD, Guo DQ, Ruan YJ, Xia DD (2015) One-pot fabrication of layered α-phase nickel- cobalt hydroxides as advanced electrode materials for pseudocapacitors. ChemPlusChem 80:181–182
5. Jeffrey WL, Bélanger D, Brousse T, Sugimoto W, Sassin MB, Crosnier O (2011) Asymmetric electrochemical capacitors — stretching the limits of aqueous electrolytes. MRS Bull 36:513–522
6. Wang J, Chang J, Wang L, Hao J (2018) One-step and low-temperature synthesis of $CoMoO_4$ nanowire arrays on Ni foam for asymmetric supercapacitors. Ionics 24:3967–3973
7. Nicolas GB, Crosnier O, Buvat G, Favier F, Brousse T (2016) Electrochemical study of aqueous asymmetric $FeWO_4/MnO_2$ supercapacitor. J Power Sources 326:695–701
8. Zhao P, Yao MQ, Ren HB, Wang N, Komarneni S (2019) Nanocomposites of hierarchical ultrathin MnO_2 nanosheets/hollow carbon nanofibers for high-performance asymmetric supercapacitors. Appl Surf Sci 463:931–938
9. Wang XZ, Su DC, Xiao YH, Xu SG, Fang SM, Cao SK (2019) Ultra-dispersed island-like Co_9S_8 nanoparticles composed of nanosheets in-situ grown on nitrogen-doped graphene for asymmetric supercapacitor. Electrochim Acta 293:419–425
10. Wei M, Wang C, Yao YB, Yu SH, Liao WH, Ren JW, Sun R, Wong CP (2019) Toward high-performance all-solid-state supercapacitors using facilely fabricated graphite nanosheet-supported $CoMoS_4$ as electrode material. Chem Eng J 355:891–900
11. Wang HP, Ma GF, Tong YC, Yang ZR (2018) Biomass carbon/polyaniline composite and WO_3 nanowire-based asymmetric supercapacitor with superior performance. Ionics 24:3123–3131
12. He XY, Zhao YH, Chen RR, Zhang HS, Liu JY, Liu Q, Song DL, Li RM, Wang J (2018) Hierarchical $FeCo_2O_4$@polypyrrole core/shell nanowires on carbon cloth for high-performance flexible all-solid-state asymmetric supercapacitors. ACS Sustain Chem Eng 6: 14945–14954
13. Zhao YH, He XY, Chen RR, Liu Q, Liu JY, Song DL, Zhang HS, Dong HX, Li RM, Zhang ML, Wang J (2018) Hierarchical $NiCo_2S_4$@$CoMoO_4$ core/shell heterostructures nanowire arrays as advanced electrodes for flexible all-solid-state asymmetric supercapacitors. Appl Surf Sci 453:73–82
14. Zhao YH, He XY, Chen RR, Liu Q, Liu JY, Yu J, Li JQ, Zhang HS, Dong HX, Zhang ML, Wang J (2018) A flexible all-solid-state asymmetric supercapacitors based on hierarchical carbon cloth@$CoMoO_4$@NiCo layered double hydroxide core-shell heterostructures. Chem Eng J 352:29–38
15. Lang JW, Kong LB, Liu M, Luo YC, Kang L (2010) Asymmetric supercapacitors based on stabilized α-$Ni(OH)_2$ and activated carbon. J Solid State Electrochem 14:1533–1539
16. Yang PH, Ding Y, Lin ZY, Chen ZW, Li YZ, Qiang PF, Ebrahimi M, Mai WJ, Wong CP, Wang ZL (2014) Low-cost high-performance solid-state asymmetric supercapacitors based on MnO_2 nanowires and Fe_2O_3 nanotubes. Nano Lett 14:731–736
17. Aguilera L, Leyet Y, Garcia RP, Hernández EP, Passos RR, Pocrifka LA (2017) Cabbage-like α-$Ni(OH)_2$ with a good long-term cycling stability and high electrochemical performances for supercapacitor applications. Chem Phys Lett 677:75–79
18. Li HL, Liu SQ, Huang CH, Zhou Z, Li YH, Fang D (2011) Characterization and supercapacitor application of coin-like β-nickel hydroxide nanoplates. Electrochim Acta 58:89–94
19. Pichamon S, Pawin I, Atiweena K, Tanut P, Peerapan D, Pinit K (2017) Hybrid energy storage of battery-type nickel hydroxide and supercapacitor-type graphene: redox additive and charge storage mechanism. Sustain Energ Fuels 1:275–279
20. Vijaykumar S, Muralidharan G (2014) Electrochemical supercapacitor behavior of α-$Ni(OH)_2$ nanoparticles synthesized via green chemistry route. J Electroanal Chem 727:53–58
21. Lokhande PE, Chavan US (2018) Nanoflower-like $Ni(OH)_2$ synthesis with chemical bath deposition method for high performance electrochemical applications. Mater Lett 218:225–228
22. Khan Y, Hussain S, Söderlind F, Käll PO, Abbasi MA, Durrani SK (2012) Honeycomb β-$Ni(OH)_2$ films grown on 3D nickel foam substrates at low temperature. Mater Lett 69:37–40
23. Xiong X, Ding D, Chen D, Waller G, Bu Y, Wang Z, Liu M (2015) Three-dimensional ultrathin $Ni(OH)_2$ nanosheets grown on nickel foam for high-performance supercapacitors. Nano Energy 11:154–161
24. Tian X, Cheng C, Qian L, Zheng B, Yuan H, Xie S, Xiao D, Choi MMF (2012) Microwave-assisted non-aqueous homogenous precipitation of nanoball-like mesoporous α-$Ni(OH)_2$ as a precursor for NiO_x and its application as a pseudocapacitor. J Mater Chem 22: 8029
25. Lukatskaya MR, Dunn B, Gogotsi Y (2016) Multidimensional materials and device architectures for future hybrid energy storage. Nat Commun 12647:1–5
26. Liu TY, Zhang F, Song Y, Li Y (2017) Revitalizing carbon supercapacitor electrodes with hierarchical porous structures. J Mater Chem A 5:17705–17733
27. Inal IIG, Holmes SM, Banford A, Aktas Z (2015) The performance of supercapacitor electrodes developed from chemically activated carbon produced from waste tea. Appl Surf Sci 357:696–703
28. Thubsuang U, Laebang S, Manmuanpom N, Wongkasemjit S, Chaisuwan T (2017) Tuning pore characteristics of porous carbon monoliths prepared from rubber wood waste treated with H_3PO_4 or NaOH and their potential as supercapacitor electrode materials. J Mater Sci 52:6837–6855
29. Lei W, Han LL, Xuan CJ, Lin RQ, Liu HF, Xin HL, Wang D (2016) Nitrogen-doped carbon nanofibers derived from polypyrrole coated bacterial cellulose as high-performance electrode materials for

supercapacitors and Li-ion batteries. Electrochim Acta 210:130–137
30. Chen H, Liu D, Shen ZH, Bao BF, Zhao SY, Wu LM (2015) Functional biomass carbons with hierarchical porous structure for supercapacitor electrode materials. Electrochim Acta 180:241–225
31. Zhang WL, Xu JH, Hou DX, Yin J, Liu DB, He YP, Lin HB (2018) Hierarchical porous carbon prepared from biomass through a facile method for supercapacitor applications. J Colloid Interface Sci 530: 338–344
32. Sherstha S, Mustain WE (2010) Properties of nitrogen-functionalized ordered mesoporous carbon prepared using polypyrrole precursor. J Electrochem Soc 157:B1665–B1672
33. Chen LF, Zhang XD, Liang HW, Kong MG, Guan QF, Chen P, Wu ZY, Yu SH (2012) Synthesis of nitrogen-doped porous carbon nanofibers as an efficient electrode material for supercapacitors. ACS Nano 6:7092–7102
34. Hu ZX, Li SS, Chen PP, Yu WD, Li RC, Shao XF, Lin WR, Yuan DS (2016) N, P-co-doped carbon nanowires prepared from bacterial cellulose for supercapacitor. J Mater Sci 5:2627–2633
35. Wang B, Li XL, Luo B, Yang JX, Wang XJ, Song Q, Chen SY, Zhi LJ (2013) Pyrolyzed bacterial cellulose: a versatile support for lithium ion battery anode materials. Small 9:2399–2404
36. Chen LF, Huang ZH, Liang HW, Gao HL, Yu SH (2014) Three-dimensional heteroatom-doped carbon nanofiber networks derived from bacterial cellulose for supercapacitors. Adv Funct Mater 24: 5104–5111
37. Yan J, Fan ZJ, Sun W, Ning GQ, Wei T, Zhang Q, Zhang RF, Zhi LJ, Wei F (2012) Advanced asymmetric supercapacitors based on $Ni(OH)_2$/graphene and porous graphene electrodes with high energy density. Adv Funct Mater 22:2632–2641
38. Chen XA, Chen XH, Zhang FQ, Yang Z, Huang SM (2013) One-pot hydrothermal synthesis of reduced graphene oxide/carbon nanotube/α-$Ni(OH)_2$ composites for high performance electrochemical supercapacitor. J Power Sources 243:556–557
39. Lee JW, Ahn T, Soundararajan D, Koc JM, Kim JD (2011) Non-aqueous approach to the preparation of reduced graphene oxide/α-$Ni(OH)_2$ hybrid composites and their high capacitance behavior. Chem Commun 47:6305–6307
40. Yang YF, Cheng D, Chen SJ, Guan YL, Xiong J (2018) Construction of hierarchical $NiCo_2S_4$@$Ni(OH)_2$ core-shell hybrid nanosheet arrays on Ni foam for high-performance aqueous hybrid supercapacitors. Electrochim Acta 193:116–127
41. Ede SR, Anantharaj S, Kumaran KT, Mishra S, Kundu S (2017) One step synthesis of Ni/$Ni(OH)_2$ nano sheets (NSs) and their application in asymmetric supercapacitors. RSC Adv 7:5898–5911
42. Li XM, Qiao YQ, Wang CH, Shen TD, Zhang XY, Wang HC, Li YS, Gao WM (2019) MOF-derived Co/C nanocomposites encapsulated by $Ni(OH)_2$ ultrathin nanosheets shell for high performance supercapacitors. J Alloys Compd 770:803–812
43. Wang DW, Guan B, Li Y, Li DD, Xu ZY, Hu YF, Wang YQ, Zhang HH (2018) Morphology-controlled synthesis of hierarchical mesoporous α-$Ni(OH)_2$ microspheres for high-performance asymmetric supercapacitors. J Alloys Compd 737:238–247
44. Wang PY, Li YN, Li SD, Liao XQ, Sun SM (2017) Water-promoted zeolitic framework-67 transformation to Ni-Co layered double hydroxide hollow microsphere for supercapacitor electrode material. J Mater Sci Mater Electron 28:9221–9227
45. Li M, Yang HX, Wang YH, Wang LW, Chu PK (2018) Core-shell $CoMoO_4$@$Ni(OH)_2$ on ordered macro-porous electrode plate for high-performance supercapacitor. Electrochim Acta 283:538–547
46. Bai X, Liu Q, Liu JY, Zhang HS, Li ZS, Jing XY, Liu PL, Wang J, Li RM (2017) Hierarchical Co_3O_4@$Ni(OH)_2$ core-shell nanosheet arrays for isolated all-solid state supercapacitor electrodes with superior electrochemical performance. Chem Eng J 315:35–45